Check for updates

ADVANCED FUNCTIONAL MATERIALS
www.afm-journal.de

Ferrocene Derivatives Enable Ultrasensitive Perovskite Photodetectors with Enhanced Reverse Bias Stability

Eunyoung Hong, William D. J. Tremlett, Lucy Hart, Beier Hu, Zhuoran Qiao, Patipan Sukpoonprom, Sarah Fearn, Edoardo Angela, Matilde Brunetta, Demosthenes C. Koutsogeorgis, Nikolaos Kalfagiannis, Davide Nodari, Martyn A. McLachlan, Piers R. F. Barnes, Artem A. Bakulin, Nicholas J. Long, and Nicola Gasparini**

Despite the great potential of lead-halide perovskite photodetectors for broadband photodetection, ion migration in perovskites and parasitic charge injection from adjacent layers remain major challenges, ultimately leading to device failure. Here, the novel use of an ultra-thin layer of ferrocenyl-bis-phenyl-2-carboxylate ($FcPhc_2$) is demonstrated as a hole-blocking layer. It is shown that $FcPhc_2$ creates an energetic barrier between the perovskite and the electron transport layer, significantly reducing hole injection from the Ag contact. This improvement results in an ultralow noise spectral density of 1.2×10^{-14} A $Hz^{-1/2}$, and a high specific detectivity of 8.1×10^{12} Jones at −0.5 V and 740 nm. In addition, $FcPhc_2$ effectively inhibits I^- oxidation induced by injected holes and reduces formed I_2 on the perovskite surface, enhancing reverse bias stability. The increase in detectivity and stability does not compromise the high response speed of $FcPhc_2$-based devices that operate on the scale of 150 ns and 1.3 MHz at −0.5 V in photo- and electrical-responses.

1. Introduction

Recent advancements in broadband photodetection, which fundamentally rely on photon-to-electron transduction across a broad spectrum of wavelengths, from ultraviolet (UV) to near-infrared (NIR), have led to growing demand for high resolution and rapid response, as well as long-term stability of photodiodes, which are crucial in hyperspectral light detection and ranging (LiDAR) systems,[1,2] imaging,[3–5] and optical communications.[6,7] Lead-halide perovskite (LHP) photodiodes have emerged as an attractive option for broadband photodetectors due to their remarkable optoelectronic properties, such as compositional tuneability,[8,9] high charge carrier mobility,[10,11] extended charge carrier lifetimes,[12] long diffusion lengths,[13] and low-temperature solution processability,[14,15] all of which have considerable potential for commercial applications. Nonetheless, several challenges remain in devices with LHPs, primarily stemming from their inherent material instability. For example, their sensitivity to moisture and oxygen promotes the deprotonation of organic cations, leading to the decomposition of the absorber layer.[16–18] Moreover, various environmental stressors, including electric fields and light

E. Hong, W. D. J. Tremlett, L. Hart, B. Hu, Z. Qiao, P. Sukpoonprom, D. Nodari, A. A. Bakulin, N. J. Long, N. Gasparini
Department of Chemistry
Imperial College London
London W12 0BZ, UK
E-mail: n.long@imperial.ac.uk; n.gasparini@imperial.ac.uk

L. Hart, P. R. F. Barnes
Department of Physics
Imperial College London
London SW7 2AZ, UK

The ORCID identification number(s) for the author(s) of this article can be found under https://doi.org/10.1002/adfm.202424556

© 2025 The Author(s). Advanced Functional Materials published by Wiley-VCH GmbH. This is an open access article under the terms of the Creative Commons Attribution License, which permits use, distribution and reproduction in any medium, provided the original work is properly cited.

DOI: 10.1002/adfm.202424556

P. Sukpoonprom
Department of Material Science and Engineering
Vidyasirimedhi Institute of Science and Technology (VISTEC)
Rayong 21210, Thailand

S. Fearn, E. Angela, M. Brunetta, M. A. McLachlan
Department of Materials
Imperial College London
London SW7 2AZ, UK

D. C. Koutsogeorgis, N. Kalfagiannis
School of Science and Technology
Nottingham Trent University
Nottingham NG11 8NS, UK

16163028, 2026, 21, Downloaded from https://advanced.onlinelibrary.wiley.com/doi/10.1002/adfm.202424556 by Imperial College London, Wiley Online Library on [20/05/2026]. See the Terms and Conditions (https://onlinelibrary.wiley.com/terms-and-conditions) on Wiley Online Library for rules of use; OA articles are governed by the applicable Creative Commons License

exposure, can lead to a higher density of ionic defects and greater ion migration.[19–27] This often results in significant hysteresis and device degradation, particularly under reverse bias, as holes can tunnel to the perovskite layer from the Ag electrode and interact with mobile iodine (I_2) interstitials.[19,20] The resultant I_2 are unstable and mobile, meaning that they are prone to escape the perovskite layer. Additionally, it has been reported that I_2 can traverse C_{60} and oxidize the Ag contact, causing shunting and substantial recombination losses within the device.[19]

Significant efforts have been made to address these key issues and improve perovskite photodetectors (PPDs). These include material-driven strategies, wherein compositional or additive engineering mitigates bulk and surface defects of the perovskite layer,[8,9,28] and interface engineering,[29,30] which improves energy level alignment between neighboring layers or raises energy barriers to promote charge transfer and suppress undesired charge injection. Beyond these approaches, using a thin buffer layer has been proven crucial in preventing the injection of charge carriers from the adjacent electrodes into the perovskite layer in the absence of light.[31–33] Any deficiencies in the performance of the blocking layer increase the leakage current and thus the dark current density (J_D). Recently, it has been reported that a range of materials, including bathocuproine (BCP), bathophenanthroline (BPhen),[34] atomic layer deposition-processed tin oxide (ALD-SnO_2), and lithium fluoride (LiF),[20] can effectively suppress shunting paths and simultaneously enhance reverse bias stability. While charge-blocking layers are beneficial in reducing J_D in PPDs, their design requires meticulous consideration to avoid substantial energy level mismatches or chemical instability issues that could impede fast charge extraction, limiting the response speed and specific detectivity (D^*). Ferrocene (Fc) has been extensively studied for its exceptional electronic and electrochemical properties, primarily due to its mild and reversible one-electron oxidation to the stable ferrocenium (Fc^+) cation.[35] Recently, Fc-based complexes used as an interlayer in photovoltaic devices have been shown to facilitate electron transfer through the Fc motif and effectively passivate perovskite surface traps.[36–39] However, there are no such examples to date of Fc-derived compounds for the passivation of PPDs.

In this work, we introduce an ultra-thin layer of a Fc-derived compound between the perovskite and the electron transport layer (ETL). Two Fc derivatives, ferrocenyl-bis-thiophene-2-carboxylate ($FcTc_2$) and ferrocenyl-bis-phenyl-2-carboxylate ($FcPhc_2$), are evaluated as materials for supplementary hole-blocking layer (HBL), besides the conventional BCP buffer layer. We find that the secondary energetic barrier effectively blocks the parasitic hole injection from the Ag contact to the perovskite layer, allowing for a substantially reduced J_D of 2.4 $\times$ 10^{-9} A cm^{-2} and a noise spectral density (S_n) of 1.2 $\times$ 10^{-14} A $Hz^{-1/2}$ at −0.5 V. This subsequently improved key figures of merit, with the $FcPhc_2$ device achieving a record-high specific detectivity (D^*) of 8.1 $\times$ 10^{12} Jones at 740 nm, and a linear dynamic range (LDR) of 117 dB at −0.5 V. Although the energetic barrier between the conduction band minimum (CBM) of the perovskite and the lowest unoccupied molecular orbital (LUMO) of the Fc derivatives impedes charge transfer under short circuit conditions, this is ameliorated under reverse bias conditions, resulting in PPDs with a high response speed of 150 ns and 1.3 MHz at −0.5 V in the optical and electrical responses. Lastly, we found that the Fc-based compounds can effectively reduce ion migration across the perovskite interface by promoting the reduction of generated I_2, which ultimately enhanced reverse bias device stability under in-operando conditions.

2. Results and Discussion

2.1. Interfacial Functionalization by Ferrocene Derivatives

A summary of the p-i-n PPD's configuration is given in **Figure 1a**, where the device was built on a patterned indium tin oxide (ITO) substrate. The mixed-cation perovskite of $Cs_{0.05}(FA_{5/6}MA_{1/6})_{0.95}Pb(I_{0.85}Br_{0.15})_3$ treated with MACl (CsFAMA, where MA is methylammonium and FA is formamidinium) was sandwiched between the hole transport layer (HTL) of [2-(3,6-dimethoxy-9H-carbazol-9-yl)ethyl]phosphonic acid (MeO-2PACz) and the ETL of C_{60}. Figure S1 (Supporting Information) illustrates the full device stack's cross-sectional scanning electron microscopy (SEM) image, which consists of glass/ITO/MeO-2PACz/perovskite/C_{60}/BCP/Ag. Here, a thin layer of the Fc derivatives was introduced between the perovskite layer and the ETL. Figure 1a depicts the chemical structures of the tailored Fc-based molecules, where the thiophene moieties couple to the Fc framework via ester linkers in $FcTc_2$, while $FcPhc_2$ is functionalized with phenyl rings. The ultraviolet–visible (UV–Vis) absorption spectra of $FcTc_2$ and $FcPhc_2$ as a thin film and in solution are depicted in Figures S2–S4 (Supporting Information). The Fc-derivative layer is not visible in the complete device stack (Figure 1c), but the depth profile analysis, performed with time-of-flight secondary ion mass spectrometry measurements, confirms its presence as a distinct layer lying above the perovskite layer (Figure 1d and Figure S5, Supporting Information). The thickness of both Fc-derivative layers is less than 1 nm, as indicated by additional ellipsometry measurements (Figure S6, Supporting Information). These thin layers will allow electron extraction via tunneling from the perovskite CBM to silver (Ag)9 electrode. Optical and morphological investigations show a negligible impact of the Fc derivatives on the optical properties and crystallinity of the perovskite layer (Figures S7–S9, Supporting Information). The electrical properties of the Fc-derivative interlayers were investigated using air photoemission spectroscopy (APS), and the relevant energy level diagram is shown in Figure 1b. The optical bandgaps (E_g) were obtained from the UV–Vis absorption spectra (Figures S4, S7, S10, Supporting Information), while the energies of the highest occupied molecular orbital (HOMO) and the valence band maximum (VBM) are demonstrated in Figure S11 (Supporting Information). The corresponding energies of CBM (LUMO) were determined by subtracting VBM (HOMO)

N. Kalfagiannis
Department of Materials Science and Engineering
University of Ioannina
Ioannina 45110, Greece
P. R. F. Barnes, A. A. Bakulin, N. Gasparini
Centre for Processable Electronics
London SW7 2AZ, UK

© 2025 The Author(s). Advanced Functional Materials published by Wiley-VCH GmbH

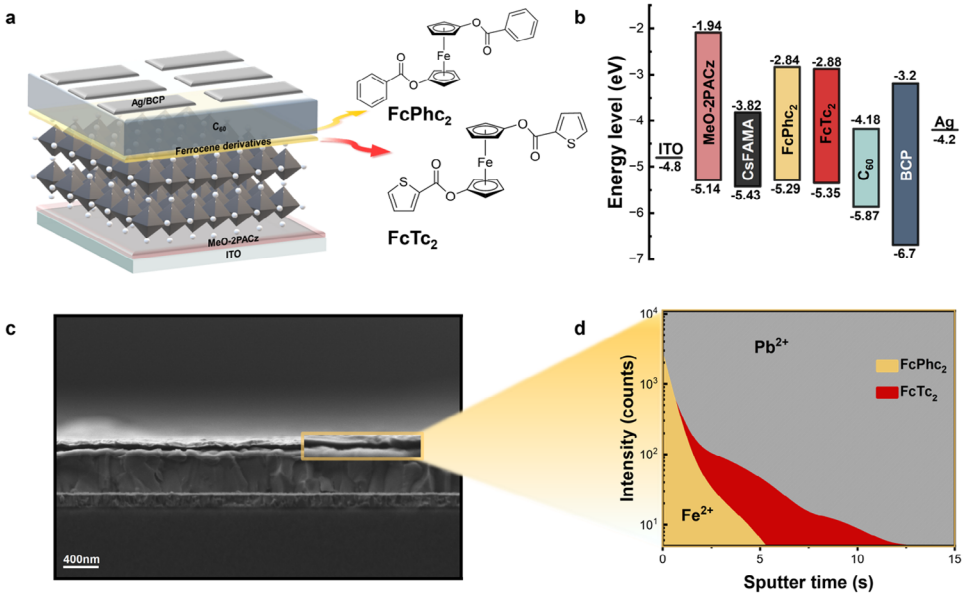


Figure 1. Perovskite photodiodes and Fc derivatives. a) An overview of device structure with Fc derivatives as an interlayer between the perovskite and C_{60}. b) Schematic energy diagram of the complete device stack. c) Cross-sectional image of the device with a Fc-derivative layer. d) Time-of-flight secondary ion mass spectrometry (ToF-SIMS) investigated the depth profile of the ITO/MeO-2PACz/perovskite/Fc derivative samples. The ion beam was focused on the Fc-derivative layer. While the Pb^{2+} signal is related to the perovskite, the Fe^{2+} signals are illustrated in yellow for $FcPhc_2$ and red for $FcTc_2$. The initial few nanometers of ion distribution reveal the interface between the perovskite and Fc-derivative layers.

from the E_g (Table S1, Supporting Information). The schematic energy level alignment of the entire device stack shows that the Fc derivatives have shallower HOMO levels than the adjacent layers, resulting in an interface energy offset ($\Delta\Phi_{HOMO}$) between the perovskite and Fc layers.

2.2. Ferrocene Derivatives as a Supplementary Barrier

To study the impact of the functionalized Fc-derived layers on mitigating parasitic charge injection, we measured the current density–voltage ($J-V$) characteristics under light and dark conditions. The J_D was recorded at −0.5 V to facilitate charge extraction while reducing potential contributions from mobile ions which have been observed at higher voltages.[40] The corresponding statistical J_D values are presented in Figure S12a (Supporting Information). The triple cation-based control devices in this study are referred to as the reference, while those modulated with the Fc derivatives are labelled as $FcTc_2$ and $FcPhc_2$. On average, the J_D of the reference was 2.4×10^{-8} A cm^{-2}, but the presence of the injection barrier created by the $FcTc_2$ or $FcPhc_2$ interlayers reduced the value to 1.2×10^{-8} and 2.4×10^{-9} A cm^{-2}, respectively, an order of magnitude improvement from the reference. Notably, $FcPhc_2$ was confirmed to have this effect across different perovskite compositions, as it consistently exhibited a lower J_D than the reference in our $MAPbI_3$ system (Figure S12b, Supporting Information). The reduction in J_D is mainly due to the $\Delta\Phi_{HOMO}$ at the perovskite/Fc-derivative interface, which effectively restricts the flow of holes from the C_{60} into the active layer. In particular, FcPh2 showed the highest barrier due to its deeper HOMO levels (5.35 eV) compared to FcTc2 (5.29 eV). Under reverse bias, this effect would be intensified as the potential barrier steepens. Similar trends were observed in the noise current, random fluctuation in electrical signals that restricts the detection of the smallest optical signals, which suggests the prevalence of shot noise in our perovskite system (see Table S2, Supporting Information). **Figure 2b** illustrates the noise spectral density (S_n) with a reverse bias of −0.5 V, obtained with stabilized current values over time.[41,42] For the reference, a S_n of 3.1×10^{-13} A Hz$^{-1/2}$ was achieved, with a marginally lower value of 1.6×10^{-13} A Hz$^{-1/2}$ for $FcTc_2$ devices, and a further decline to 1.2×10^{-14} A Hz$^{-1/2}$ in $FcPhc_2$ devices (see Figure S13, Supporting Information for the S_n in the low frequency regions). This led to further analysis of the sensitivity of our PD system, focusing on two key performance metrics for PPDs, which are predominantly influenced by the noise level.

Specific detectivity (D^*), a numerical metric that quantifies the sensitivity of a device at a certain wavelength, is the ability to discern subtle changes in light intensity accurately. The D^* can be determined as follows:

$$D^* = \frac{\sqrt{A\Delta f}R}{S_n} \quad (1)$$

where A is the active area of the PD, Δf is the electrical bandwidth, and R is the responsivity. Here, the R, closely related to external quantum efficiency (EQE), is a measure of wavelength-dependent electrical current generated in response to incident optical power. Figure S14 (Supporting Information) depicts the spectral response scanned across the UV-to-NIR spectrum at −0.5 V. All devices exhibited their peak responses at 740 nm, with values of 0.47, 0.38, and 0.46 A W^{-1} for the reference, $FcTc_2$ and $FcPhc_2$, respectively. We obtained a peak D^* value of 3.2×10^{11} Jones for the reference, but it increased with the incorporation of

© 2025 The Author(s). Advanced Functional Materials published by Wiley-VCH GmbH

16163028, 2026, 21, Downloaded from https://advanced.onlinelibrary.wiley.com/doi/10.1002/adfm.202424556 by Imperial College London, Wiley Online Library on [20/05/2026]. See the Terms and Conditions (https://onlinelibrary.wiley.com/terms-and-conditions) on Wiley Online Library for rules of use; OA articles are governed by the applicable Creative Commons License

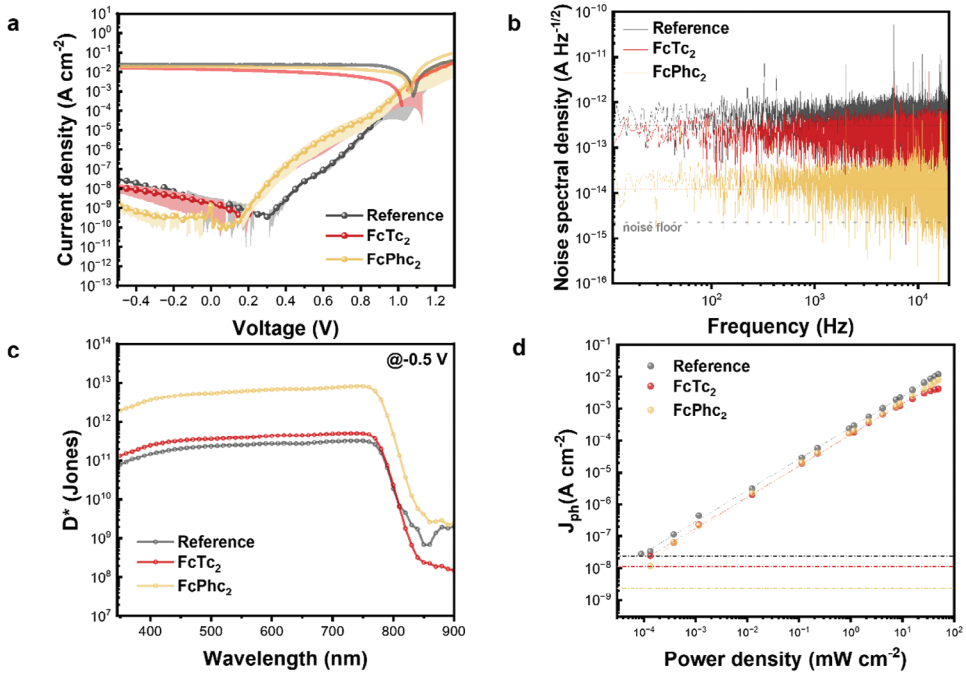


Figure 2. Average J_D and PD performance of the reference, $FcTc_2$ and $FcPhc_2$. a) *J–V* characteristics measured in the dark and under 1 sun illumination at −0.5 V. For each condition, we determined the average J_D values from 18 measurements, represented by dots, and the corresponding standard deviation by filled bands. b) Noise spectral density (S_n) as a function of frequency measured at −0.5 V. c) Specific detectivity (D^*) and d) J_{ph} as a function of various light intensities measured under 530 nm LED at −0.5 V. The dashed lines illustrate the J_D for each condition, while the J_{ph} values at various light intensities are shown as dots.

the Fc-derivative layer, reaching 5.0×10^{11} Jones for $FcTc_2$, and nearly two orders of magnitude for $FcPhc_2$, to 8.1×10^{12} Jones (Figure 2c), which is similar to that of commercially available Si-based photodiodes.[43,44] It is to be noted that the enhanced D^* of the $FcPhc_2$ and $FcTc_2$ devices stemmed from their lower noise levels, potentially expanding the operational range by allowing the device to detect weaker light intensities.

Here, linear dynamic range (LDR), the range within which photocurrent is linearly proportional to input light intensities, is determined by extrapolating photocurrent density (J_{ph}) at a given incident optical power.

$$LDR = 20 \cdot \log\frac{J_{max}}{J_{min}} \tag{2}$$

J_{max} and J_{min} are the upper and lower limits of J_{ph} that fall into the linear region, where the photocurrent changes in proportion to incident light intensity. Figure 2d shows the dynamic ranges and the relevant dark current floors of our PD system, measured at −0.5 V under 530 nm light.

The $FcPhc_2$-based devices demonstrated an extended LDR of 117 dB relative to $FcTc_2$ and the reference devices, which only showed linear dependence on intensity over 102 dB and 113 dB, respectively. This was primarily due to the lower signal detection threshold in the $FcPhc_2$ device resulting in a significantly reduced J_{min}, which aligns with its lower S_n and J_D.

2.3. Ferrocene Derivatives as a Reverse-Bias Limited Transporting Layer

In addition to achieving high detectivity, a fast temporal resolution or response speed is essential for various PD applications, such as real-time signal detection and wireless optical communications.[6,7] Here, we investigated dynamic photo responses to examine the effects of interfacial functionalization with Fc derivatives. **Figure 3a,b** illustrates the transient photocurrent (TPC) decays for the reference, $FcTc_2$ and $FcPhc_2$ devices, all excited at 515 nm optical pulses under short-circuit and reverse-bias conditions, respectively. We determined the response speed by measuring the time required for the photocurrent to decay from 90% to 10% of its peak response. As shown in Figure 3a, the reference demonstrated a fall time (τ_{fall}) of 148 ns under no bias, whereas the $FcTc_2$- and $FcPhc_2$-based devices exhibited sluggish decay times of 304 and 293 ns, respectively. We associate the longer decay times for the devices with Fc-derived modification to Fc LUMO levels lying nearly 1 eV shallower than the CBM of the reference, creating an electron injection barrier.

The time-resolved photoluminescence (TR-PL) spectra in Figure S15 (Supporting Information) show that the signals from $FcTc_2$ and $FcPhc_2$ decay more rapidly than that of the reference. This suggests that the energetic barrier of the Fc-derivative layer impedes charge transport, likely causing an electron accumulation at the interface.[45] The presence of the charge injection barrier is further evidenced by the photovoltaic characteristics of the entire stack devices under 1 sun (AM 1.5 G) and 530 nm illumination conditions (Figures S16, S17, Supporting Information).

© 2025 The Author(s). Advanced Functional Materials published by Wiley-VCH GmbH

16163028, 2026, 21, Downloaded from https://advanced.onlinelibrary.wiley.com/doi/10.1002/adfm.202424556 by Imperial College London, Wiley Online Library on [20/05/2026]. See the Terms and Conditions (https://onlinelibrary.wiley.com/terms-and-conditions) on Wiley Online Library for rules of use; OA articles are governed by the applicable Creative Commons License

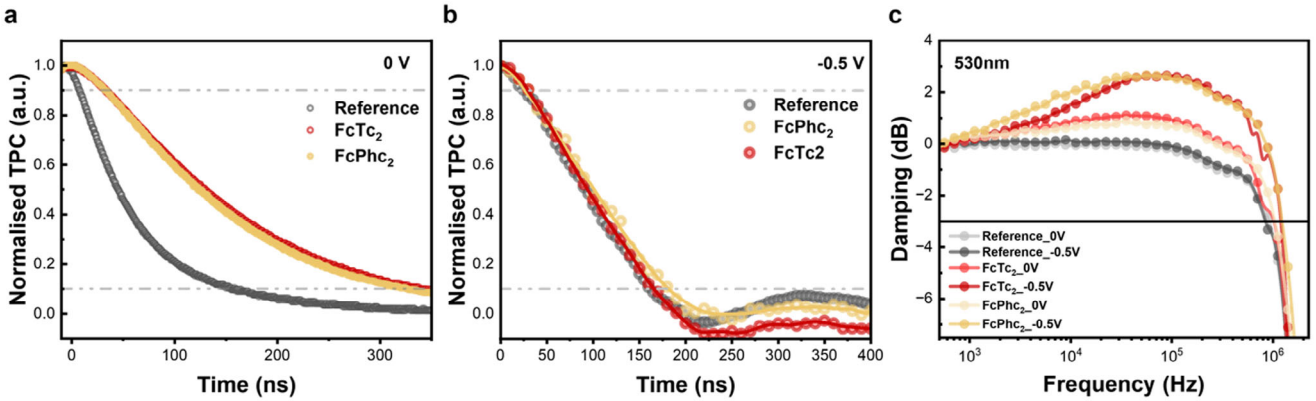


Figure 3. Transient photocurrent response of the reference, $FcTc_2$ and $FcPhc_2$ devices. a) TPC decay kinetics of the PPDs measured using a 515 nm pulse laser with a repetition rate of 5 kHz without bias. b) TPC decay kinetics under the same conditions as 3a, but measured at −0.5 V. Here, the devices were additionally perturbed by a source meter. c) Optical bandwidth under 530 nm LED with/without −0.5 V reverse bias.

However, a significant acceleration of τ_{fall} was observed for both $FcTc_2$ and $FcPhc_2$ at a reverse bias of −0.5 V, reducing their values to 133 and 150 ns, respectively, while the τ_{fall} reduced only slightly to 133 ns in the reference devices, while the rise times are similar between the devices due to similar charge generation (see Figure S18, Supporting Information for the transient photoresponse under a 530 nm LED).

Likewise, the bias-dependent responses of both $FcTc_2$ and $FcPhc_2$ were clearly demonstrated in their optical bandwidth by monitoring the electrical frequency spectrum of the devices that a system can support. The cut-off frequency ($f_{-3\,dB}$), defined as the frequency at which the response of a device drops by -3 dB from its initial signal amplitude, was measured under different illumination wavelengths (Figure S19, Supporting Information). Figure 3c depicts the $f_{-3\,dB}$ curves obtained under 530 nm illumination, with each point representing the optical signal intensity at the corresponding frequency relative to that measured at 500 Hz. The $FcTc_2$- and $FcPhc_2$-based devices both showed a significant increase in their response toward the high-frequency end of the spectrum before the cut-off. These relative increases were more pronounced when reverse bias was applied, which also extended the bandwidth limits beyond 1 MHz. The higher photo-response at higher frequencies was observed over a range of visible illumination wavelengths (Figure S19 and Table S3, Supporting Information). However, the reference exhibited a rather constant $f_{-3\,dB}$ of 0.9 MHz regardless of the bias applied. Similarly to the transient response observed in the time domain, we attribute the bias dependency in the $FcTc_2$- and $FcPhc_2$-functionalized devices to charge carrier accumulation under stronger electric fields. To support our hypothesis, we simulated the optical bandwidths for our PD systems.

2.4. Equivalent Circuit Model

To explain the observed frequency- dependent photo-responses of the devices in this study, we propose an equivalent circuit model to encapsulate the core physical processes in the PPDs. Our equivalent circuit is based on concepts proposed by Moia et al. but modified to account for only the most relevant aspects of the device architecture.[46] The model predicts a PPD's current response to large changes in light intensity or voltage, however, it does not attempt to describe all possible aspects of the device physics but is restricted to the processes illustrated in **Figure** 4a.

The model assumes that the electrostatic potential within a PPD is dominated by the distribution of mobile ionic charged defects within the perovskite active layer, which are represented by the upper branch of the equivalent circuit model shown in Figure 4b. The capacitors C_A and C_B represent the ionic accumulation/depletion regions at the perovskite/MeO-2PACz and perovskite/FcR_2/C_{60} interfaces, respectively, while C_g and R_{ion} are the geometric capacitance and ionic resistance of the perovskite layer. Changes in the capacitive accumulation and depletion of ionic charge (Q_{ion} represents the *change* in accumulated ionic charge relative to equilibrium) at perovskite/FcR_2/C_{60} interface alters the height of the energetic barrier to electron transfer (collection) across the interface by an amount $V_{gB} = Q_{ion}/C_B + JR_S$. The resulting change in the perovskite/FcR_2/C_{60} barrier is coupled to the electron collection current density, J_{col}, across the interface in the lower branch of the equivalent circuit using a bipolar transistor element where the base voltage V_{gB} modulates the interface's transconductance. The response of this branch to an external voltage (V) or photogeneration current (J_{gen}) stimulus determines the value of the voltage V_{gB}, which gates the bipolar n-p-n transistor representing the extraction (collection) of electrons from the perovskite layer.

In the lower branch of the circuit, we consider processes involving electronic carriers. The parallel combination of the current source and diode represents the generation (J_{gen}) and trap-assisted recombination (J_{rec}) of electrons and holes in the bulk of the perovskite. We placed these processes on the illuminated side of the device by the HTL/perovskite interface, where the majority of carriers are generated. Since the measurements here are performed at short-circuit or reverse bias, we neglect interfacial recombination processes as minority carrier densities at the perovskite/transport layer interfaces will be low. To account for the finite mobility of electrons in the perovskite, we have included a resistance to electron transport, R_T, which describes the change in the electron quasi-Fermi level between the bulk of the perovskite and the interface given the current density of electrons

© 2025 The Author(s). Advanced Functional Materials published by Wiley-VCH GmbH

16163028, 2026, 21, Downloaded from https://advanced.onlinelibrary.wiley.com/doi/10.1002/adfm.202424556 by Imperial College London, Wiley Online Library on [20/05/2026]. See the Terms and Conditions (https://onlinelibrary.wiley.com/terms-and-conditions) on Wiley Online Library for rules of use; OA articles are governed by the applicable Creative Commons License

16163028, 2026, 21, Downloaded from https://advanced.onlinelibrary.wiley.com/doi/10.1002/adfm.202424556 by Imperial College London, Wiley Online Library on [20/05/2026]. See the Terms and Conditions (https://onlinelibrary.wiley.com/terms-and-conditions) on Wiley Online Library for rules of use; OA articles are governed by the applicable Creative Commons License

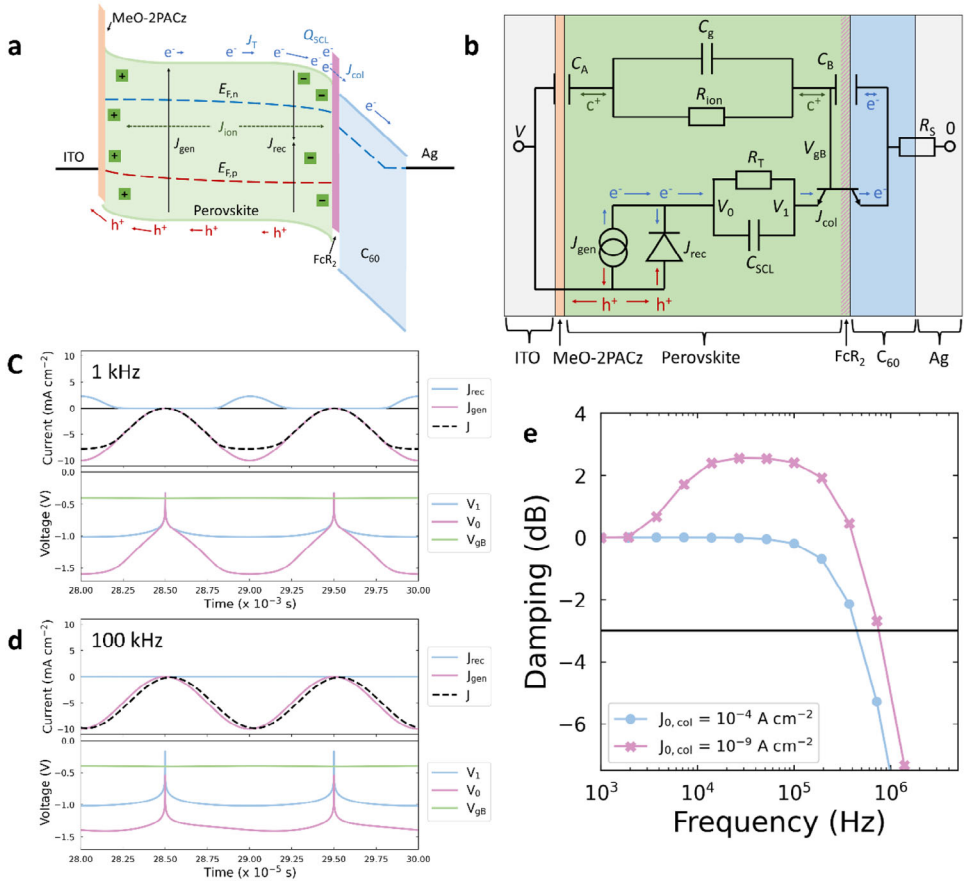


Figure 4. Simulated photo-response using a perovskite photodiodes equivalent circuit model. a) Energy level diagram of the photodiode at short circuit under illumination with photogeneration current density J_{gen}, where FcR_2 refers to either $FcTc_2$ or $FcPhc_2$. Collection of electrons and holes and their respective quasi-Fermi levels are indicated (e^-, h^+, $E_{F,n}$, and $E_{F,p}$). b) Equivalent circuit model of the same device. The upper circuit "branch" describes the transport (R_{ion}) and accumulation (C_A and C_B) of mobile ionic defects (c^+) within the perovskite layer. The lower branch describes the photogeneration (J_{gen}), recombination (J_{rec}), transport (R_T), accumulation (C_{SCL}), and collection (J_{col}) of electrons and holes in the device. Upper panels show the time dependence of the recombination current (J_{rec}) when the photogeneration current (J_{gen}) is modulated at c) 1 kHz and d) 100 kHz for the device with $J_{0,col} = 10^{-9}$ A cm^{-2}. Lower panels show the time dependence of V_0, V_1 and V_{gB}. e) Simulated photo-response with and without the FcR_2 layer using the equivalent circuit model shown in (b). A low collection saturation current density for the transistor (giving a high collection resistance) of $J_{0,col} = 10^{-9}$ A cm^{-2} was used to simulate the presence of the FcR_2 layer, and a much higher value (and thus lower resistance) of $J_{0,col} = 10^{-4}$ A cm^{-2} was used to simulate the reference device without the FcR_2 layer.

transported to the perovskite/FcR_2/C_{60} interface, J_T. In parallel with this, we have placed a capacitor, C_{SCL}, to describe the accumulation of electrons in the interfacial region when electron collection across the interface is poor. The variable resistance to charge collection across the perovskite/FcR_2/C_{60} is parameterized by the saturation current density of the transistor element $J_{0,col}$. To model the presence of the Fc derivatives, we assume that they act as a barrier to electron extraction, as is suggested by the lower J_{SC} and fill factor of these devices (Figure S16, Supporting Information), and thus reduce the value of $J_{0,col}$ when compared to the reference device. To understand the effect of this, we considered the equation describing the current through the transistor:

$$J_{trans} = J_{0,col} \exp\left(\frac{q\left(V_{gB} - JR_s\right)}{nkT}\right)\left[1 - \exp\left(-\frac{q(V_1 - JR_s)}{nkT}\right)\right] \quad (3)$$

in which n is the ideality factor of the interface, q is the charge of the electron, k is Boltzmann's constant, T is the temperature, J is the total current through the device and R_S is the series resistance of the electrodes and MeO-2PACz. Consequently, the smaller $J_{0,inj}$ becomes, the more negative V_1 must be to support the same current flow through across the interface. Physically, this corresponds to a greater accumulation of charge in the device, increasing bulk recombination losses and eventually leading to the formation of an electron accumulation region at the perovskite/C_{60} interface.[47] This space charge layer in the perovskite is represented by the capacitor C_{SCL}. We note that C_{SCL} and R_T should strictly be functions of the photocurrent and applied bias, as their values will depend upon the electron density and electrostatic potential in the perovskite. However, we found that we were able to reproduce the observed behavior of the devices using constant values of both parameters (all model parameters are provided in Table S4, Supporting Information). As noted above, the electronic charge stored in the space charge layer is

© 2025 The Author(s). Advanced Functional Materials published by Wiley-VCH GmbH

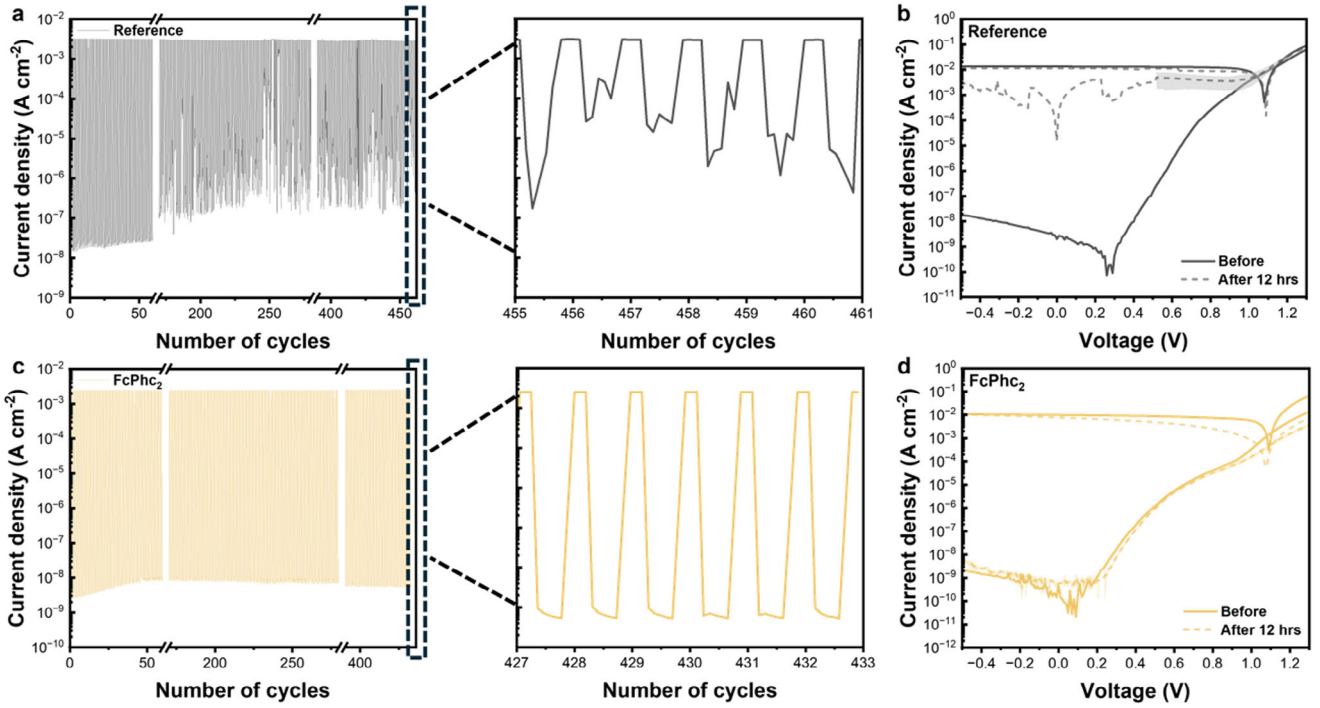


Figure 5. Continuous monitoring of the current levels of the reference and $FcPhc_2$ device under operando conditions. The unencapsulated devices were subjected to a reverse bias of −0.5 V and measured in ambient air (20 °C and 58% RH) using a 530 nm LED with square pulses at a repetition rate of 15 mHz. a,c) Illustrative on-off cycles and b,d) *J–V* curves before and after the stability test for the reference and $FcPhc_2$ devices, respectively. The average J_D values measured after the test are depicted as dots, while the corresponding standard deviations are represented as filled bands.

small compared to the ionic charge and so does not affect the electrostatics of the device (and thus is not directly coupled to the upper branch of the circuit) but can significantly affect the device's electronic response to high-frequency stimuli, as we show in Figure 4c–e.

Figure 4e shows the results of simulating the bandwidth measurements at an applied bias of −0.5 V (full details of the simulation and measurement protocol are given in Note S1, Supporting Information). We see that decreasing $J_{0,col}$ leads to the observed "bump" in the frequency response of the device, while also reducing the peak-to-peak amplitude of the current at low frequencies (see Figure S20, Supporting Information), consistent with the observed loss in J_{SC} for the devices containing the Fc derivatives. To understand the origin of the "bump" in the frequency response, we show the contributions of the recombination and generation currents (J_{rec} and J_{gen}, respectively) to the total current for the device with $J_{0,col} = 10^{-9}$ A cm^{-2} at frequencies of 10^3 Hz and 10^5 Hz in Figure 4d,e, as well as the time dependence of the voltages V_0, V_1 and V_{gB} (see Figure S21 (Supporting Information) for plots showing the device with $J_{0,col} = 10^{-4}$ A cm^{-2}). These figures demonstrate that the increase in the current at high frequencies is due to a reduction in the recombination current through the device. At low frequencies, the accumulation of charge on C_{SCL} increases the voltage driving recombination across the diode ($V(t)$–V_0), because the impedance of C_{SCL} is high. Thus, the total photocurrent decreases since more current is lost to recombination. At high frequencies, C_{SCL} does not have time to fully charge or discharge (the impedance of the C_{SCL} is low), so there is a lower potential difference across the diode, reducing J_{rec} and increasing the photocurrent. This effect is less significant when $J_{0,col}$ is larger, as a smaller value of V_1 (and thus $V_0 = V_1 + Q_{SCL}/C_{SCL}$) can deliver the same total current (Figure S21, Supporting Information).

2.5. Ferrocene Derivatives as a Perovskite Shield against Degradation

Ion migration under reverse bias and illumination conditions has been shown to form localized clusters of defects and trigger chemical reactions or ion build-up at the interfaces between the perovskite and adjacent transport layers, which are ultimately associated with substantial increases in J_D, inefficient charge collection, and device failure over time.[21,48] Although C_{60} and BCP can function as hole injection barriers, they are not sufficient to entirely prevent these adverse consequences of ion migration. Here, we investigated the effect of the Fc-functionalized interlayer on mitigating performance degradation and improving the stability of the PPDs, which is critical to realizing their commercial viability.

Given that PDs are predominantly used in indoor applications, it is suitable to conduct testing under low illumination and dark conditions to mimic real-world indoor lighting environments. We measured *J–V* scans for the reference and $FcPhc_2$ devices before and after the continuous on/off cycles at −0.5 V under 530 nm illumination (49.3 mW cm^{-2}) in ambient air (**Figure 5** and Table S5, Supporting Information). Here we used low-frequency pulses (15 mHz) to monitor for variations in

© 2025 The Author(s). Advanced Functional Materials published by Wiley-VCH GmbH

16163028, 2026, 21, Downloaded from https://advanced.onlinelibrary.wiley.com/doi/10.1002/adfm.202424556 by Imperial College London, Wiley Online Library on [20/05/2026]. See the Terms and Conditions (https://onlinelibrary.wiley.com/terms-and-conditions) on Wiley Online Library for rules of use; OA articles are governed by the applicable Creative Commons License

photo- and dark current, as the latter, in the order of 10^{-11} A in our system, requires a significant acquisition time (Figure S13, Supporting Information).[30] As shown in Figure 5a,b, the reference exhibited a substantial increase in J_D during light-off periods, nearly by five orders of magnitude, despite a negligible decline in photocurrent. In contrast, the $FcPhc_2$-treated device maintained its initial J_D on average, experiencing only a minor decay of less than one order of magnitude over 400 cycles (Figure 5c,d). Notably, $FcPhc_2$ consistently showed a stable photocurrent response in nitrogen, in an environment that reflected an ideal encapsulation (Figure S22 and Table S5, Supporting Information). We believe the improved stability stemmed from the Φ_{HOMO} of $FcPhc_2$, which can effectively block holes introduced from the metal Ag, thus preventing the oxidation of I^- ions. Furthermore, we found $FcPhc_2$ to have the potential to inhibit the loss of I^- ions from the perovskite layer through the reduction of I_2 formed on the perovskite surface. $FcPhc_2$ undergoes complete oxidation when an equivalent of I_2 is added. This was indicated by the broadening and disappearance of cyclopentadienyl (Cp) and phenyl peaks in the ^{1}H NMR spectrum due to the formation of the paramagnetic Fe^{3+} complex (Figures S23–S25, Supporting Information). When I_2 is added to $FcPhc_2$, the Fe^{2+} center is oxidized to Fe^{3+} (i.e., the ferrocene moiety is oxidized to ferrocenium) due to the lower redox potential of $FcPhc_2$ compared to I_2. This leads to stronger magnetic fields between these unpaired electrons and neighboring nuclei, causing these nuclei to have more rapid relaxation times (T_1 and T_2), and overall resulting in peak broadening. These larger local magnetic fields of these unpaired electrons also have a larger impact on the external magnetic field, which results in shifting resonance frequencies. Diamagnetic compounds (those with no unpaired electrons) have slower relaxation times and lower magnetic fields, and so their peaks are more resolved and their shifts more predictable.

Moreover, the redox potential of $FcPhc_2$ (114 mV vs Fc/Fc^+) is lower than that of I_2 (193 mV vs Fc/Fc^+) confirming the ability of I_2 to oxidize $FcPhc_2$ (Figures S26–S29 and Table S6, Supporting Information). Similar observations with other Fc and related derivatives on perovskite devices have also suggested the suppression of I_2 migration through a catalytic redox process, with the formation of a FcI-type complex and subsequent re-reduction through the oxidation of Pb defects.[49,50]

3. Conclusion

In summary, we have developed high-performance PPDs with enhanced reverse bias stability by incorporating an ultra-thin layer of Fc-derived compounds between the perovskite and C_{60}. Our results have demonstrated three key roles of the Fc-derived interlayer as a supplementary charge injection barrier, which reduced the J_D as low as 2.4×10^{-9} A cm^{-2} and a S_n of 1.2×10^{-14} A Hz$^{-1/2}$, leading to high D^* of 8.1×10^{12} Jones at 740 nm. We found that the band bending is enhanced under reverse bias relative to the zero-bias condition, resulting in the PPDs with a high response speed of 150 ns and 1.3 MHz at −0.5 V in the optical and electrical responses, respectively. This is supported by modelling suggesting a reduction in the recombination current through the device under reverse bias conditions. Finally, $FcPhc_2$ acts as a perovskite shield against device degradation by blocking hole traversing from the Ag contact to the light absorber and suppressing I^- ion migration through the reduction of formed I_2. Consequently, we have achieved a PPD with a stable J_D over 400 continuous on/off cycles under reverse bias. Our findings thus indicate the versatility of Fc derivatives and propose a new strategy for improving PPD performance while maintaining both efficiency and stability under reverse bias.

4. Experimental Section

Materials: Perovskite solutions were prepared by using PbI_2 (99.99%, TCI), $PbBr_2$ (>98.0%, TCI) and organic halide salts of MAI (>99.9%, GreatCell Solar), FAI (>99.9%, GreatCell Solar), MACl (99.0%, Sigma-Aldrich) and CsI (99.99%, Sigma Aldrich). [2-(3,6-dimethoxy-9H-carbazol-9-yl)ethyl]phosphonic acid (MeO-2PACz) was purchased from TCI (98.0%). The bathocuproine (BCP) was purchased from Lumtec (>99.5%). All anhydrous solvents were purchased from Sigma Aldrich. More details about ferrocenyl-bis-thiophene-2-carboxylate ($FcTc_2$) and ferrocenyl-bis-phenyl-2-carboxylate ($FcPhc_2$) are presented in the Supporting Information.

Device Fabrication: PPDs were fabricated in an inverted p-i-n structure on glass substrates patterned with indium tin oxide (ITO). The substrates were sequentially cleaned with acetone and 2-propanol (IPA) by ultrasonication for 10 min in each solvent. They were then dried with N_2 and treated with UV-ozone for 15 min. The hole transporting layer (HTL), perovskite, and Fc-derivative layers were spin-coated in a N_2-filled glove box. For the control device, an HTL of MeO-2PACz dissolved in ethanol (1 mM) was spun on ITO at 3000 rpm for 30 s and dried at 100 °C for 10 min. The perovskite layers were synthesized with varying compositions: 1) For 1.2 M $Cs_{0.05}(FA_{5/6}MA_{1/6})_{0.95}Pb(I_{0.85}Br_{0.15})_3$, the perovskite precursor solution with an 1% excess of PbI_2 was prepared by mixing cations (Cs, MA and FA) and halides (I and Br) in a DMSO:DMF (4:1/v:v) mixed solvent. 10 mol% MACl was then added to the precursor solution and stirred at 60 °C for 1 h. The perovskite solution was deposited in a two-step process, first at 1000 rpm for 1 s, followed by at 5000 rpm for 27 s. 150 mL of chlorobenzene (CB) was dripped during the second spin-coating. The film was then annealed at 100 °C for 30 min. 2) For 1.5 M $MAPbI_3$ (MAPI), the perovskite solution was prepared by dissolving MAI and PbI_2 in a solvent mixture of DMSO:DMF (1:9/v:v), which was then heated at 60 °C for 60 min. The preheated perovskite solution was spin-coated at 4000 rpm for 20 s, during which 0.4 mL of diethyl ether was dripped onto the film at 6s after the start. Subsequently, the perovskite film was annealed at 100 °C for 30 min. Regarding the optimal thickness of the modified Fc interlayer, we experimentally found that a layer that was too thin fails to completely cover the entire perovskite layer, while the movement of charge carriers was hindered by an excessively thick layer. Thus, 0.3 mg mL^{-1} of the Fc derivatives were used to enable direct tunnelling of charge carriers and prevent undesired charge injection from the contacts (see more in Figure S30, Supporting Information). For the devices treated with $FcTc_2$ and $FcPhc_2$, 0.3 mg mL^{-1} of the Fc derivatives were dissolved in CB, and dynamically spin-coated onto the perovskite layer at 4000 rpm for 40 s. The samples were then dried at 100 °C for 4 min. To finish the stack of the device with a pixel area of 0.045 cm^2, about 40 nm of C_{60}, 10 nm of BCP, and 100 nm of Ag were thermally evaporated as the ETL, HBL, and top electrode, respectively.

Perovskite Characterizations: For the UV–Vis spectroscopy measurements, quartz/perovskite, quartz/perovskite/Fc derivative, and quartz/Fc derivative samples were prepared, and the absorption spectra were measured by using an Agilent Cary 60 UV–Vis spectrophotometer. Kelvin probe coupled with ambient photoemission spectroscopy (KP-APS) was performed on ITO/perovskite, ITO/perovskite/Fc derivative, ITO/MeO-2PACz and ITO/Fc derivative samples with a KP Technology SKP5050 Scanning Kelvin Prove and an APS02 Air Photoemission System. Time-resolved PL measurements were carried out using a Horiba Delta Flex (PPD-900, Horiba Scientific) operated at repetition rate of 1 MHz with low-fluence irradiation. The glass/perovskite/Fc derivative samples were excited using a 467 nm continuous wave (CW) laser diode with a pulse duration of <200 ps (NanoLED). ToF-SIMS measurements were conducted on ITO/MeO-2PACz/perovskite/Fc-derivative samples, sputtering from the

© 2025 The Author(s). Advanced Functional Materials published by Wiley-VCH GmbH

16163028, 2026, 21, Downloaded from https://advanced.onlinelibrary.wiley.com/doi/10.1002/adfm.202424556 by Imperial College London, Wiley Online Library on [20/05/2026]. See the Terms and Conditions (https://onlinelibrary.wiley.com/terms-and-conditions) on Wiley Online Library for rules of use; OA articles are governed by the applicable Creative Commons License

Fc layer into the perovskite film. The samples were depth profiled using an IONTOF ToF-SIMS V instrument. A 25 keV Bi^+_3 ion beam in HCBM was used to analyze the sample, over a 150 × 150 μm^2 area with 128 × 128 pules. The samples were sputtered using a 10 keV $Ar_{15000}{}^+$ GCIB over an area of 400 × 400 μm^2. Final sputter crater depths were measured using the Zygo NexView optical interferometer. Both top-view SEM and device cross-sectional images were taken on a field SEM (FE-SEM) Gemini 1 Zeiss Sigma 300. The images were acquired by secondary electron detector (SE2) under an accelerating voltage of 2.00 kV while keeping a low working distance. Spectroscopic ellipsometry measurements were performed on Si/Fc derivative films using a variable angle spectroscopic ellipsometer (in the spectral range 192–1690 nm) to extract accurate optical constants. The thickness was determined using the Cauchy model in the region of transparency for both materials.

PPD Characterization: *J–V* measurements were conducted with a Keithley 4200 Source-Measurement unit (scan rate of 25 mV s^{-1}), and an Oriel Instruments Solar Simulator in the range of −0.5 to +1.3 V. The measurements were carried out in ambient air and under AM 1.5G light of 100 mW cm^{-2}, calibrating its intensity using a Si reference cell. Noise power spectral density was measured by a Keithley 4200 Source Measurement unit and a digital oscilloscope (Siglent, SDS6054A) coupled with a high-speed current amplifier (Femto, DHPCA-100) to provide a variable gain. Responsivity was measured in ambient air using an integrated system from a Quantum Design PVE300 at a modulation frequency of 90 Hz after signal calibration with a Si reference photodiode. For linear dynamic range measurements, a 530 nm continuous LED was pulsed by a function generator (ThorLabs DC2200) and focused on the perovskite device. To attenuate the light intensity, a selection of neutral density filters were placed between the device and the lamp. Transient photocurrent data were obtained by using a digital oscilloscope (RIGOL DS4024) with a 515 nm laser as the excitation source and a pulse duration of 190 fs. The laser repetition frequency was set to 5 kHz, with an intensity of 2 μJ cm^{-2}. For the bias-dependence TPC measurements, a 2450 SourceMeter was used to apply reverse bias to the encapsulated devices. Impedance spectroscopy measurements were carried out using a STAT-I-400 potentiostat. The devices were subjected to a small perturbation of 20 mV and were measured using a 530 nm LED, specifically under V_{OC} conditions. The scanning process was carried out within the frequency range of 10 MHz to 10 Hz. For stability measurements, the unencapsulated devices were subjected to a reverse bias of −0.5 V in ambient air (20 °C and 58% RH). A Keithley 4200 Source Measure unit was used to record the current over time. The devices were placed under the 530 nm LED with square pulses at a repetition rate of 15 mHz (powered by a function generator ThorLabs DC2200).

Supporting Information

Supporting Information is available from the Wiley Online Library or from the author.

Acknowledgements

E.H. and W.D.J.T. contributed equally to this work. N.K.G. thanks the Engineering and Physics Science Research Council (EPSRC) (EP/T028513/1) and the European Union under grant agreement number 101172797. N.J.L. acknowledges Imperial College London for funding via the Sir Edward Frankland BP Chair endowment, an Impact Acceleration Award and the Deep-Tech Prime programme, and is also grateful for a Royal Society Wolfson Research Merit award. L.J.F.H. and P.R.F.B. acknowledge the EPSRC ATIP project (EP/TO28513/1). B.H. and A.A.B. acknowledge support from UKRI/EPSRC (ActionSpec, Grant Ref: EP/X030822/1).

Conflict of Interest

The authors declare no conflict of interest.

Data Availability Statement

The data that support the findings of this study are available from the corresponding author upon reasonable request.

Keywords

ferrocene, interlayer, noise current, perovskite photodetectors, reverse bias stability

Received: December 12, 2024
Revised: February 28, 2025
Published online: March 20, 2025

[1] A. Morteza Najarian, M. Vafaie, A. Johnston, T. Zhu, M. Wei, M. I. Saidaminov, Y. Hou, S. Hoogland, F. P. García de Arquer, E. H. Sargent, *Nat. Electron.* **2022**, *5*, 511.
[2] A. Morteza Najarian, M. Vafaie, B. Chen, F. P. García de Arquer, E. H. Sargent, *Nat. Rev. Phys.* **2024**, *6*, 219.
[3] B. Wang, C. Zhang, B. Zeng, C. Y. Wu, C. Xie, D. Wu, Y. X. Zhou, L. B. Luo, *J. Phys. Chem. Lett.* **2021**, *12*, 2930.
[4] Y. Duan, R. Yu, H. Zhang, W. Yang, W. Xie, Y. A. Huang, Z. Yin, *Adv. Mater.* **2024**, *36*, 2313946.
[5] D. Wu, Y. Zhang, C. Liu, Z. Sun, Z. Wang, Z. Lin, M. Qiu, D. Fu, K. Wang, *Adv. Devices Instrum.* **2023**, *4*, 0006.
[6] C. Bao, J. Yang, S. Bai, W. Xu, Z. Yan, Q. Xu, J. Liu, W. Zhang, F. Gao, C. Bao, W. Zhang, J. Yang, S. Bai, W. Xu, Z. Yan, F. Gao, Q. Xu, J. Liu, *Adv. Mater.* **2018**, *30*, 1803422.
[7] D. Zheng, T. Pauporté, *Adv. Funct. Mater.* **2024**, *34*, 2311205.
[8] F. Furlan, D. Nodari, E. Palladino, E. Angela, L. Mohan, J. Briscoe, M. J. Fuchter, T. J. Macdonald, G. Grancini, M. A. McLachlan, N. Gasparini, *Adv. Opt. Mater.* **2022**, *10*, 2201816.
[9] E. Hong, D. Nodari, F. Furlan, E. Angela, J. Panidi, M. A. McLachlan, N. Gasparini, *Adv. Opt. Mater.* **2024**, *12*, 2302712.
[10] H. Oga, A. Saeki, Y. Ogomi, S. Hayase, S. Seki, *J. Am. Chem. Soc.* **2014**, *136*, 13818.
[11] L. M. Herz, *Annu. Rev. Phys. Chem.* **2016**, *67*, 65.
[12] C. Wehrenfennig, G. E. Eperon, M. B. Johnston, H. J. Snaith, L. M. Herz, C. Wehrenfennig, G. E. Eperon, M. B. Johnston, H. J. Snaith, L. M. Herz, *Adv. Mater.* **2014**, *26*, 1584.
[13] S. D. Stranks, G. E. Eperon, G. Grancini, C. Menelaou, M. J. P. Alcocer, T. Leijtens, L. M. Herz, A. Petrozza, H. J. Snaith, *Science* **2013**, *342*, 341.
[14] Y. Xu, Q. Lin, *Appl. Phys. Rev.* **2020**, *7*, 11315.
[15] L. Dou, Y. M. Yang, J. You, Z. Hong, W. H. Chang, G. Li, Y. Yang, *Nat. Commun.* **2014**, *5*, 5404.
[16] Q. Wang, B. Chen, Y. Liu, Y. Deng, Y. Bai, Q. Dong, J. Huang, *Energy Environ. Sci.* **2017**, *10*, 516.
[17] B. P. Kore, M. Jamshidi, J. M. Gardner, *Mater. Adv.* **2024**, *5*, 2200.
[18] R. Xing, Z. Li, W. Zhao, D. Wang, R. Xie, Y. Chen, L. Wu, X. Fang, *Adv. Mater.* **2024**, *36*, 2310248.
[19] F. Jiang, Y. Shi, T. R. Rana, D. Morales, I. E. Gould, D. P. McCarthy, J. A. Smith, M. G. Christoforo, M. Y. Yaman, F. Mandani, T. Terlier, H. Contreras, S. Barlow, A. D. Mohite, H. J. Snaith, S. R. Marder, J. D. MacKenzie, M. D. McGehee, D. S. Ginger, *Nat. Energy* **2024**, *9*, 1275.
[20] N. Li, Z. Shi, C. Fei, H. Jiao, M. Li, H. Gu, S. P. Harvey, Y. Dong, M. C. Beard, J. Huang, *Nat. Energy* **2024**, *9*, 1264.
[21] Z. Xu, R. A. Kerner, S. P. Harvey, K. Zhu, J. J. Berry, B. P. Rand, *ACS Energy Lett.* **2023**, *8*, 513.
[22] P. Calado, A. M. Telford, D. Bryant, X. Li, J. Nelson, B. C. O'Regan, P. R. F. Barnes, *Nat. Commun.* **2016**, *7*, 13831.
[23] J. M. Ball, A. Petrozza, *Nat. Energy* **2016**, *1*, 16149.

© 2025 The Author(s). Advanced Functional Materials published by Wiley-VCH GmbH

16163028, 2026, 21, Downloaded from https://advanced.onlinelibrary.wiley.com/doi/10.1002/adfm.202424556 by Imperial College London, Wiley Online Library on [20/05/2026]. See the Terms and Conditions (https://onlinelibrary.wiley.com/terms-and-conditions) on Wiley Online Library for rules of use; OA articles are governed by the applicable Creative Commons License

[24] S. Zeiske, O. J. Sandberg, N. Zarrabi, C. M. Wolff, M. Raoufi, F. Peña-Camargo, E. Gutierrez-Partida, P. Meredith, M. Stolterfoht, A. Armin, *J. Phys. Chem. Lett.* **2022**, *13*, 7280.
[25] K. Datta, B. T. van Gorkom, Z. Chen, M. J. Dyson, T. P. A. van der Pol, S. C. J. Meskers, S. Tao, P. A. Bobbert, M. M. Wienk, R. A. J. Janssen, *ACS Appl. Energy Mater.* **2021**, *4*, 6650.
[26] A. R. Bowring, L. Bertoluzzi, B. C. O'Regan, M. D. McGehee, *Adv. Energy Mater.* **2018**, *8*, 1702365.
[27] H. Jin, E. Debroye, M. Keshavarz, I. G. Scheblykin, M. B. J. Roeffaers, J. Hofkens, J. A. Steele, *Mater. Horiz.* **2020**,*7*, 397.
[28] R. Li, J. Peng, Y. Xu, W. Li, L. Cui, Y. Li, Q. Lin, *Adv. Opt. Mater.* **2021**, *9*, 2001587.
[29] E. Angela, D. Nodari, F. Furlan, J. Panidi, M. A. McLachlan, N. Gasparini, *ACS Appl. Mater. Interfaces* **2024**, *16*, 33838.
[30] D. Nodari, L. J. F. Hart, O. J. Sandberg, F. Furlan, E. Angela, J. Panidi, Z. Qiao, M. A. McLachlan, P. R. F. Barnes, J. R. Durrant, A. Ardalan, N. Gasparini, *Adv. Mater.* **2024**, *36*, 2401206.
[31] S. Asgary, H. M. Moghaddam, A. Bahari, R. Mohammadpour, *Sol. Energy* **2021**, *213*, 383.
[32] N. Shibayama, H. Kanda, T. W. Kim, H. Segawa, S. Ito, *APL Mater.* **2019**, *7*, 31117.
[33] C. Chen, S. Zhang, S. Wu, W. Zhang, H. Zhu, Z. Xiong, Y. Zhang, W. Chen, *RSC Adv.* **2017**, *7*, 35819.
[34] N. Li, J. Lim, J. D. Azoulay, T. N. Ng, *J. Mater. Chem. C* **2020**, *8*, 15142.
[35] G. Roy, R. Gupta, S. Ranjan Sahoo, S. Saha, D. Asthana, P. C. Mondal, *Coord. Chem. Rev.* **2022**, *473*, 214816.
[36] B. Li, D. Gao, S. A. Sheppard, W. D. J. Tremlett, Q. Liu, Z. Li, A. J. P. White, R. K. Brown, X. Sun, J. Gong, S. Li, S. Zhang, X. Wu, D. Zhao, C. Zhang, Y. Wang, X. C. Zeng, Z. Zhu, N. J. Long, *J. Am. Chem. Soc.* **2024**, *146*, 13391.
[37] Z. Li, B. Li, X. Wu, S. A. Sheppard, S. Zhang, D. Gao, N. J. Long, Z. Zhu, *Science* **2022**, *376*, 6591.
[38] B. Hu, J. Zhang, Y. Yang, Y. Dong, J. Wang, W. Wang, K. Lin, D. Xia, R. Fan, *Nano Energy* **2023**, *118*, 109022.
[39] T. Webb, X. Liu, R. J. E. Westbrook, S. Kern, M. T. Sajjad, S. Jenatsch, K. D. G. I. Jayawardena, W. H. K. Perera, I. P. Marko, S. Sathasivam, B. Li, M. Yavari, D. J. Scurr, M. R. Alexander, T. J. Macdonald, S. A. Haque, S. J. Sweeney, W. Zhang, *Adv. Energy Mater.* **2022**, *12*, 2200666.
[40] R. A. Z. Razera, D. A. Jacobs, F. Fu, P. Fiala, M. Dussouillez, F. Sahli, T. C. J. Yang, L. Ding, A. Walter, A. F. Feil, H. I. Boudinov, S. Nicolay, C. Ballif, Q. Jeangros, *J. Mater. Chem. A* **2019**, *8*, 242.
[41] Y. Fang, A. Armin, P. Meredith, J. Huang, *Nat. Photonics* **2018**, *13*, 1.
[42] F. Wang, T. Zhang, R. Xie, Z. Wang, W. Hu, *Nat. Commun.* **2023**, *14*, 2224.
[43] A. Rogalski, F. Wang, J. Wang, P. Martyniuk, W. Hu, *Small Methods* **2024**, *9*, 2400709.
[44] G. Konstantatos, J. Clifford, L. Levina, E. H. Sargent, *Nat. Photonics* **2007**, *1*, 531.
[45] X. Chen, H. P. Pasanen, R. Khan, N. V. Tkachenko, C. Janáky, G. F. Samu, *J. Phys. Chem. Lett.* **2024**, *15*, 2057.
[46] D. Moia, I. Gelmetti, P. Calado, W. Fisher, M. Stringer, O. Game, Y. Hu, P. Docampo, D. Lidzey, E. Palomares, J. Nelson, P. R. F. Barnes, *Energy Environ. Sci.* **2019**, *12*, 1296.
[47] W. Xu, L. J. F. Hart, B. Moss, P. Caprioglio, T. J. Macdonald, F. Furlan, J. Panidi, R. D. J. Oliver, R. A. Pacalaj, M. Heeney, N. Gasparini, H. J. Snaith, P. R. F. Barnes, J. R. Durrant, *Adv. Energy Mater.* **2023**, *13*, 2301102.
[48] L. Bertoluzzi, J. B. Patel, K. A. Bush, C. C. Boyd, R. A. Kerner, B. C. O'Regan, M. D. McGehee, *Adv. Energy Mater.* **2021**, *11*, 2002614.
[49] Q. Chang, F. angfang Wang, W. enxin Xu, A. Wang, Y. ou Liu, J. Wang, Y. ikai Yun, S. Gao, K. Xiao, L. Zhang, L. Wang, J. Wang, W. Huang, T. Qin, *Angew. Chem.* **2021**, *133*, 25771.
[50] H. Bi, J. Liu, Z. Zhang, L. Wang, G. Kapil, Y. Wei, A. Kumar Baranwal, S. Razey Sahamir, Y. Sanehira, D. Wang, Y. Yang, T. Kitamura, R. Beresneviciute, S. Grigalevicius, Q. Shen, S. Hayase, *Adv. Sci.* **2023**, *10*, 2304790.

© 2025 The Author(s). Advanced Functional Materials published by Wiley-VCH GmbH

16163028, 2026, 21, Downloaded from https://advanced.onlinelibrary.wiley.com/doi/10.1002/adfm.202424556 by Imperial College London, Wiley Online Library on [20/05/2026]. See the Terms and Conditions (https://onlinelibrary.wiley.com/terms-and-conditions) on Wiley Online Library for rules of use; OA articles are governed by the applicable Creative Commons License